Materials Science & Engineering A 852 (2022) 143686

Contents lists available at ScienceDirect

Materials Science & Engineering A

journal homepage: www.elsevier.com/locate/msea

Post-forming, electro-plastic effect internal stress reduction in AA5754 aluminium alloy

Wenqi Liu [a], Nagore Otegi [b], Ana Orallo [b], Manex Barrenetxea [c], Iosu Aizpuru [c], Junhe Lian [a], Joseba Mendiguren [b,*]

[a] Advanced Manufacturing and Materials, Department of Mechanical Engineering, Aalto University, Espoo, 02150, Finland
[b] Mondragon Unibertsitatea, Faculty of Engineering, Mechanics and Industrial Production, Loramendi 4, Mondragon, 20500, Gipuzkoa, Spain
[c] Mondragon Unibertsitatea, Faculty of Engineering, Electronics and Informatics, Loramendi 4, Mondragon, 20500, Gipuzkoa, Spain

ARTICLE INFO

Keywords:
Springback
AA5754
Electro-plastic effect
EPE
Stamping
Deep drawing

ABSTRACT

Aluminium alloys are one of the most efficient materials for weight reduction in the car industry. However, the favourable performance of alloys conflicts with the difficulties of transforming these materials through plastic deformation processes such as stamping. Among the different issues, they are characterised by a high springback effect. Numerous authors have explored the use of the electro-plastic effect (EPE) to mitigate internal stresses and the resultant springback. However, up-scaling existing laboratory solutions to an industrial framework is a critical challenge. Therefore, in this work, the post-forming electro-plastic effect (PFEPE) is explored in AA5754 material. Stress-relaxation + PFEPE experiments were conducted using different electric pulse charge passing though the sample, and, apart from the impact on residual stresses, the potential occurrence of recrystallisation was evaluated. The results indicate that a range of pulses exists (>2000 A·ms/mm^2 and <4500 A ms/mm^2) in which a 10–30% reduction in stresses can be achieved without critically impacting the material's mechanical performance.

1. Introduction

Automotive regulations are expected to lead to weight savings of 2–10% (2025) and 20–25% (2035) in combustion engines and 10–15% (2025) and 20–30% (2035) in electric vehicles [1]. Hence, the use of high-strength steels and aluminium alloys is predicted to grow in the next few years [2]. In the case of aluminium alloys, the material's appealing performance once in the car body conflicts with the difficulties of manufacturing the material using plastic deformation processes such as stamping [3]. Aside from the reduced malleability of these alloys [4], the springback is significantly higher than in similar strength steels due to their low elastic moduli [5].

Numerous researchers have been working on different approaches to address the springback issue regarding stamping processes, for example, improved material models [6], advanced compensation strategies [7], and warm or hot forming [8,9]. One method that has received increased interest in recent years is the use of the electro-plastic effect (EPE) [10]. The idea consists of electrically assisting the material using a train of electrical pulses while plastically deforming it to reduce the required stress and subsequent springback [11]. In the last ten years, numerous researchers have presented work using this technology [12,13]. Jiang et al. were among the first to explore EPE on magnesium forming [14], rapidly followed by Liu et al. using AZ31B [15,16], Kim et al. using AZ31 [17] (this work led to several numerical models of the phenomenon [18]) and Nguyen et al. [19] with various models together with Wang et al. [20–22]. Jeong et al. [23] studied AZ91. The latest works concerning AZ31 were published by Liu et al. [24] and Wang et al. [25]. In the case of steel, Liu et al. studied EPE on TRIP800 [26], while Kim et al. [27] and Thien et al. [28]analysed several advanced high-strength complex-phase steels (1.2 GPa) and Xie et al. [29] and Kim et al. [30] studied DP980 material. Jiang et al. [31] and Khal et al. [32] evaluated SS304 stainless steel, and Egea et al. assessed 308L stainless steel in two subsequent works, [33,34]. Jeong et al. [35], among others, studied 301L and 316L materials.

Focusing on aluminium alloys, Egea et al. used 50 μs, 100–200 Hz and 11–50 A/mm^2 (30 s) pulse trains on AA1050-H18 alloy, reducing the stresses by approximately 20% [36]. Tang et al. studied AA2024-T4 using ~50–100 A/mm^2 (250 ms), 1 Hz and 5 s pulses [37,38]. Hong

* Corresponding author.
E-mail address: jmendiguren@mondragon.edu (J. Mendiguren).

https://doi.org/10.1016/j.msea.2022.143686
Received 13 May 2022; Received in revised form 21 July 2022; Accepted 22 July 2022
Available online 1 August 2022

et al. analysed AA6061-T6 at forging conditions using 75–90 A/mm^2 (0.5 s) and 2 Hz [39], while Jung et al. characterised the impact on fatigue life using 90 A/mm^2, 0.5 ms and ~10 Hz [40]. At the sheet metal-forming level, Pan et al. studied the effect of using six pulses of 86.97 A/mm^2 (240 ms) [41] for force reduction. Hammed et al. performed AA6060 alloy tensile tests with EPE using AA6060 ~500–3190 A/mm^2 (250 μs) and 300 Hz pulse trains [42], while Tiwari et al. characterised the impact on AA6063 [43]. Chen et al. recently studied the AA7xxx family with AA7150 using ~40 A/mm^2, 1000 Hz and 20–50 s pulses [44], while Zhang and Zhang studied various Al–Zn–Mg alloys using 5–55 A/mm^2 (185 μs) and 200 Hz [45,46]. In the AA5xxx family, AA5052-H32 was first studied by Kim et al. [47] in 2014 using 110 A/mm^2 (0.5 s) and 2 Hz pulse trains. The same material was used by Roh et al. [48]. Later, Kim et al. studied the same alloy using 120 A/mm^2 (0.5 s) and 0.03 Hz pulses [49] in 2017 and 50–400 A/mm^2 (0.5 s) 0.03 Hz pulses [50] in 2020. Shibkov et al. [51] studied EPE on Portevin-Le Chatelier in Al–Mg using pulses in the range of 0–50 A/mm^2. For a more detailed review of work on this topic, see reviews by Liang and Lin [52], Grimm and Mearsek [53] and Ruszkiewicz et al. [54].

Although the technology is promising at the laboratory level, it is almost impossible to control the pulse train path through a non-square blank during a stamping operation [55]. Research into hot stamping has aimed to develop solutions using current bypasses. However, these are oriented towards out-of-tooling heating. No work has been discovered regarding devices implemented into the stamping die to trigger EPE while deforming at the industrial level. The reader is referred to Refs. [56,57] for examples of existing solutions.

In view of the difficulties, we believe that the post-forming electroplastic effect (PFEPE) could be an interesting alternative. This option delivers the electrical pulse trains immediately after forming [39] rather than during plastic deforming. A literature review reveals that Kim et al. explored PFEPE on DP780 using 40–60 A/mm^2 (0.4–1.2 s) pulses [30]. Hong et al. [39] studied AA6061-T6 using 75–90 A/mm^2 (2 Hz) pulses, while Khal et al. [32] analysed the effect of 5–30 A/mm^2 (2 s) on SS304 stainless steel. Son et al. (50–100 A/mm^2, 0.25–0.75 s) [58], Li et al. [59], Gerstein et al. [60] and Zhao et al. [61] also investigated PFEPE's capabilities.

However, from the up-scaling perspective, we believe that the electrical pulses could be applied through the thickness of the blank rather than from side to side, targeting the major bending lines by including the cathode and the anode on punch and die stamping tools. However, due to mechanical press movement [62,63], and considering there is always some tool deflection at the bottom end of the forming process [64–66] and the fact that the contact pressure is critical for the forming quality [67], industrially up-scalable PFEPE would need a high-speed pulse <1 ms. We have not identified research into these characteristics for AA5754 material, which is currently one of the most used aluminium alloys in the automotive industry.

This work investigates PFEPE's capacity to reduce the internal stresses of pre-deformed AA5754H22 material. First, the base material is studied to establish the starting point. Then, Stress-relaxation + PFEPE experiments are performed, and the stress reduction is evaluated. Finally, the impact of the electrical pulse on the material base properties, including grain and sub-grain morphology, strength, and yield stress, is investigated.

2. Materials and methods

This section first presents the studied material, followed by a description of the electrical pulse train generator constructed for the study. Next, the stress-relaxation + PFEPE test experimental set-up and methodology are depicted. Finally, the methodology for evaluating PFEPE on the material's properties following deformation is presented.

Material. The material used in this study is a cold-rolled AA5754H22 aluminium alloy sheet with a thickness of 0.8 mm. The main alloying element of this material is Mg, and the approximated chemical composition is presented in Table 1.

Pulse generator. A high current discharge circuit (HCDC) was designed and constructed to generate high current (>10^3 A/mm^2) and short pulses (<1 ms). A schematic description of the HCDC is presented in Fig. 1.

The HCDC comprises three different sub-circuits: voltage adaptation, the pre-charge circuit and the discharge circuit. The voltage adaptation circuit includes an autotransformer and a three-phase diode rectifier circuit. This first step adapts the 400 V three-phase system to a variable DC voltage between 0 V and 540 V. The pre-charge circuit ensures that the discharge circuit is charged to the desired voltage before the discharge pulse is programmed. This is performed by correctly controlling the Thyristor$_1$. Finally, the discharge circuit is designed to insert a high current pulse to the device under test (DUT) by switching on the Thyristor$_2$. The discharge capacitor C2 and the Thyristor$_2$ are the most critical devices. Both devices must withstand the full current inserted into the DUT.

The DUT current could have high current-rate values (>1 kA/us) and amplitude (>10 kA), depending on the DUT resistivity. A CWT150 Rogowsky current probe from PEMUK® was used to measure the DUT current.

Using the HCDC and DUT, a pick value of 5.87 kA was obtained (for a voltage of 450 V). Under this voltage and with a C2 capacity of 2.27 mF the resulting stored energy per pulse is of 229.83 J. The pulse demonstrates a typical step increment and exponential current reduction. The approximate pulse length is 0.57 ms. In terms of electrical charge passing through the sample, a single pulse has 1.7 kA ms, measured as the area below the current-time curve.

Stress-relaxation + PFEPE test. Modified stress-relaxation tests were performed to evaluate the impact of a short high current electrical pulse in a deformed AA5754H22 sample. A schematic diagram of the testing methodology is presented in Fig. 2. Figures (a) and (b) present the reference test procedure, and Figures (c) and (d) present the stress-relaxation + PFEPE test procedure. The samples had a width of 2.5 mm in the calibrated area. A RakuTool® (WB-1250) resin was used as insulation between the sample and the machine to avoid electrical deviation in the tensile machine.

For the reference test, the sample was stretched up to 2 mm of deformation (displacement between the clamps, leading to approximately 6.25% strain) with a tensile speed of 3 mm/min. The displacement was kept constant, as demonstrated in Fig. 2b. Ideally, the resultant signal force (schematically presented in Fig. 2a) should increase when deforming the sample (up to 2 mm of deformation) and remain constant when the displacement is maintained in a fixed position (dashed line in Fig. 2a). However, due to the machine dynamics, once the displacement is kept constant, the force signal tends to decrease slightly (demonstrated in the continuous line in Fig. 2a). Several reference tests were conducted to establish the baseline for the experiment.

In the stress-relaxation + PFEPE test procedure, the sample was stretched to 2 mm, and the displacement was kept constant, following the same procedure as the reference test. However, in this case, while maintaining the displacement (Fig. 2d), an electrical pulse (or pulse train in some cases) was applied. A schematic diagram of the resultant force signal is presented in Fig. 2c. When the pulse is applied, the sample heats up due to the Joule effect [69], and due to its thermal expansion, a sudden decrease of the force signal is demonstrated (as the displacement between the clamps is kept constant). When the sample temperature dissipates and recovers at room temperature, if PFEPE has no impact, the force signal aligns with the reference signal (the dashed line in Fig. 2c). However, if PFEPE impacts the dislocation network and, therefore, the

Table 1
Approximated chemical composition of AA5754 (wt. %) [68].

Si	Fe	Cu	Mn	Mg	Cr	Zn	Ti	Al
0.40	0.40	0.10	0.50	2.60–3.60	0.30	0.20	<0.15	Bal.

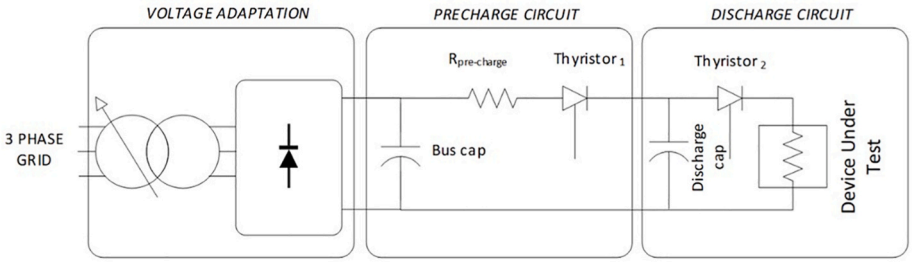

Fig. 1. High current discharge circuit (HCDC).

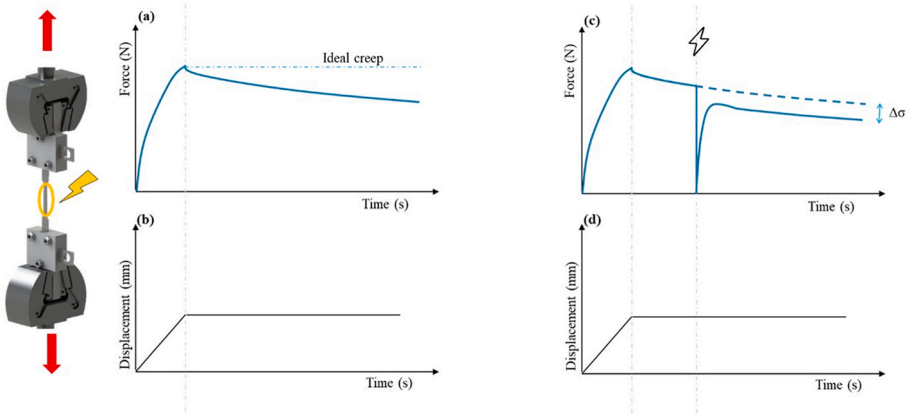

Fig. 2. Stress-relaxation + PFEPE testing methodology. Schematic representations of a) the force-time signal of the reference stress-relaxation test, b) the displacement-time signal of the reference stress-relaxation test, c) the force-time signal of the stress-relaxation + PFEPE test and d) the displacement-time signal of the stress-relaxation + PFEPE test.

internal stresses, a gap between the sample and reference behaviour is revealed. This gap, measured in force (N), can be transformed into a difference in internal stress.

Apart from the displacement and force signal, an infrared camera Optris PI400i was used to monitor the sample temperature during the entire process. Two main values were evaluated from the obtained signal. On the one hand, the peak temperature reached by the sample is recorded (and directly related to the sudden decrease in forces when applying the pulse). On the other hand, the area below the temperature-time curve is measured in K·s to represent the not only the pic temperature but also the time length of the generated temperature.

Evaluation of PFEPE's impact. The main objective of using PFEPE is to reduce the material's internal stresses using the electrical pulse to rearrange the dislocation network. However, as previous researchers have observed, EPE (with and without the apparent Joule effect) tends to accelerate material recrystallisation and grain growth in some cases. Recrystallisation is an undesired secondary effect of using PFEPE as a technological tool to reduce springback. Hence, the samples previously tested using the stress-relaxation + PFEPE methodology were studied to evaluate the potential occurrence of recrystallisation. This study was conducted on two levels. On the one hand, after unloading from the machine, the tested samples were stretched until rupture, and the sample's elasticity limit was measured. On the other hand, EBSD analyses of the samples were conducted to evaluate their microstructure.

The EBSD measurements of all the specimens were taken using rolling direction-transverse direction (RD-TD) planes. The measured surface was prepared using mechanical grinding with up to P1200 sandpaper, followed by mechanical polishing in 6 μm, 3 μm and 1 μm diamond suspension. The final preparation was 2 h in a VibroMet™ 2 vibratory polisher using colloidal silica suspension. All EBSD analyses were conducted at 30 kV acceleration voltage and a working distance of 7 mm with a 70° tilting angle. At least 8–10 investigation regions with an area of 170 μm × 120 μm and a step size of 0.16 μm were measured for each specimen. The data was summarised for both local and statistical microstructure characterisation. The MATLAB MTEX toolbox [70] was employed to analyse the grain and sub-grain microstructure.

3. Results

This section presents the results of the stress gap between the reference stress-relaxation and stress-relaxation + PFEPE tests with the temperature data. In addition, PFEPE's impact on EBSD is evaluated and the tensile test results are presented.

Fig. 3 presents the experimental results of the stress-relaxation + PFEPE tests. The stress gap is presented in a decreased percentage using the following equation:

$$\Delta\sigma = \frac{\sigma_{Ref} - \sigma_{PFEPE}}{\sigma_{Ref}} = \frac{\sigma_{Gap}}{\sigma_{Ref}} = \frac{F_{Gap}}{F_{Ref}}, \quad (1)$$

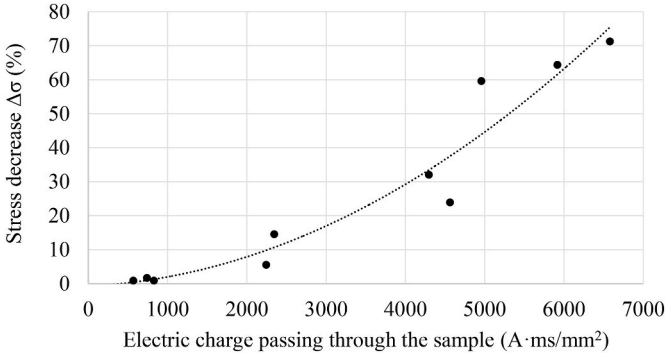

Fig. 3. Stress-relaxation + PFEPE test results. The dots represent the experimental results, and the dashed line gives a tendency approximation.

where σ_{Ref} corresponds to the stress value of the reference stress-relaxation test, and σ_{PFEPE} is the stress value after the electrical pulse and temperature dissipation (Fig. 2). Therefore, σ_{Gap} represents the stress gap between the reference stress-relaxation test and the stress-relaxation + PFEPE test. The same value can be obtained starting from the force data of the reference stress-relaxation test, F_{Ref}, and the gap between both force signals, F_{Gap}.

It should be noted that given the maximum electrical charge passing through the sample of one pulse is 1.7 kA ms, and the sample cross-section is 2 mm^2, the electric charge passing through the sample density of one pulse is 850 A ms/mm^2. In order to do this calculation, following the same terminology as previous authors, not skin-effect has been taken into account and the whole sample section has been considered. If the initial objective had been to introduce the necessary electrical charge passing through the sample in a single pulse, a pulse train would be required to achieve >850 A ms/mm^2 pulses. In such cases, the minimum length between each pulse was applied, and the entire electrical signal was recorded and considered for the electrical charge passing through the sample measurement. Using this technique, pulse trains with energies between 850 A ms/mm^2 and 6578 A ms/mm^2 were tested.

Due to the Joule effect generated by the electricity passing through the sample, the sample temperature increases during the test. The peak sample temperatures for the different experiments are presented in Fig. 4.

The thermal temperature-time value illustrated in Fig. 5 is a representative value of the amount of thermal temperature-time value introduced (or generated) in the sample.

The results given in Figs. 2–5 represent the experimental data obtained during the test. However, as discussed in the methodology section (Evaluation of PFEPE's impact), additional testing was conducted to evaluate PFEPE's impact on the material's properties. The yield stress was calculated from the conducted tensile test, and the results are presented in Fig. 6.

It should be noted that all the tested samples had a pre-strain of 2 mm (approximately 6.25% of strain). Therefore, should the electrical pulse not affect the microstructure, the sample yield strength would match the material hardening to 6.25% of uniaxial elongation. Should the pulse have an effect, the strength would vary (expectedly reduced). Hence, in Fig. 6, an extra point has been added at 0 A ms/mm^2 of ~184 ± 6 MPa, being the yield strength of the material after 2 mm (6.25%) of uniaxial elongation.

To analyse the microstructure of the different samples, three samples were studied using EBSD: a 2 mm pre-strained sample without electrical pulses (labelled Reference), a sample with an electrical pulse train of 2243 A ms/mm^2 and a sample with an electrical pulse train of 6578 A ms/mm^2 (as this is in the range where the greatest decrease in mechanical properties is demonstrated, Fig. 6). The EBSD measurements

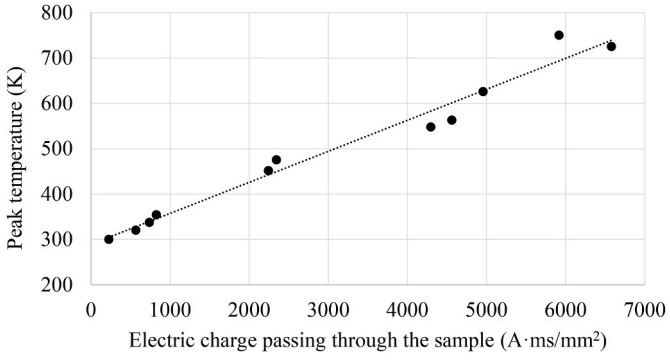

Fig. 4. Stress-relaxation + PFEPE test peak temperature results. The dots represent the experimental results, and the dashed line gives a tendency approximation.

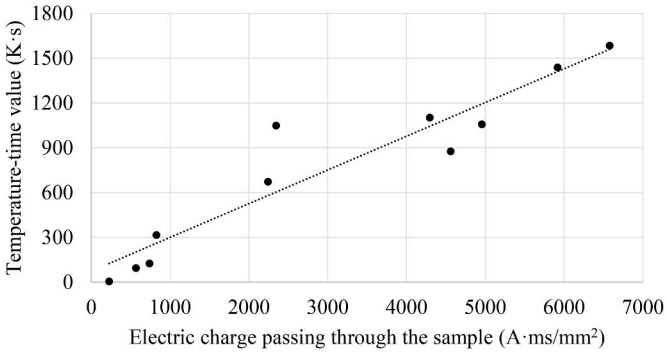

Fig. 5. Stress-relaxation + PFEPE test thermal temperature-time value results. The dots represent the experimental results, and the dashed line gives a tendency approximation.

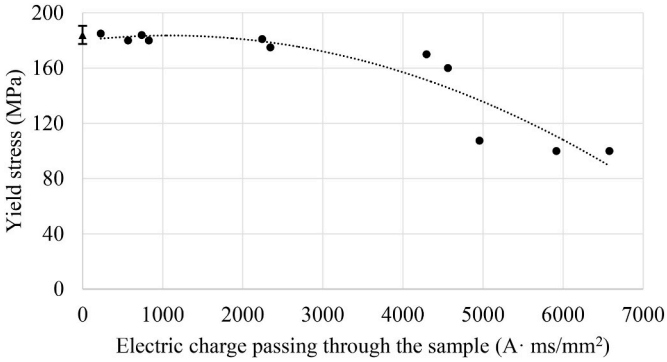

Fig. 6. Post-PFEPE tensile test results. The dots represent the experimental results, and the dashed line gives a tendency approximation.

demonstrate that the indexed phase is the pure aluminium phase. To distinguish the grains, the high-angle grain boundaries (HAGBs) are defined as 15°, while the sub-grain boundaries of 2–15°, known as the low-angle grain boundaries (LAGBs), are also investigated. The EBSD measurements obtained more than 2000 grains for each sample. For a detailed examination of the grain and sub-grain features, an example of each sample is presented in Fig. 7, including the crystal orientation maps, grain kernel average misorientation (KAM) maps and inner grain orientation spread (GOS) maps with the grain and sub-grain boundaries. The normal direction (ND) inverse pole figure (IPF) is used as the colour coding for the crystal orientation maps. The secondary order neighbouring points are considered to calculate the KAM. The inner GOS at each point is defined as the misorientation angle between its crystal orientation and the involved grain mean orientation. Therefore, the local GOS could be larger than 15° in the heterogeneously deformed grains.

The microstructural results were analysed statistically, including the grain size, shape, orientation, boundary misorientation and inner grain misorientation. The statistical analyses of the microstructural features considered all complete grains within the measurement area. For the statistical analysis, 4778 grains were evaluated for the reference sample, 2323 grains for the 2243 A ms/mm^2 sample, and 2314 grains for the 6578 A ms/mm^2 sample, as listed in Table 2. The statistical results are given in Fig. 8. The grain feature distribution is characterised according to Liu and Lian et al. [71,72]. Generally, the area fraction, defined as the equivalent grain diameter, is used for the grain size analysis (Fig. 8a). The grain shape distribution is also indicated with the area fraction, including the grain shape factor (the aspect ratio between minor and major equivalent ellipse axes, Fig. 8-b) and the grain shape tilt angle (the angle between the major equivalent ellipse axis and RD, Fig. 8c). The correlated misorientation angle is considered for both LAGBs and

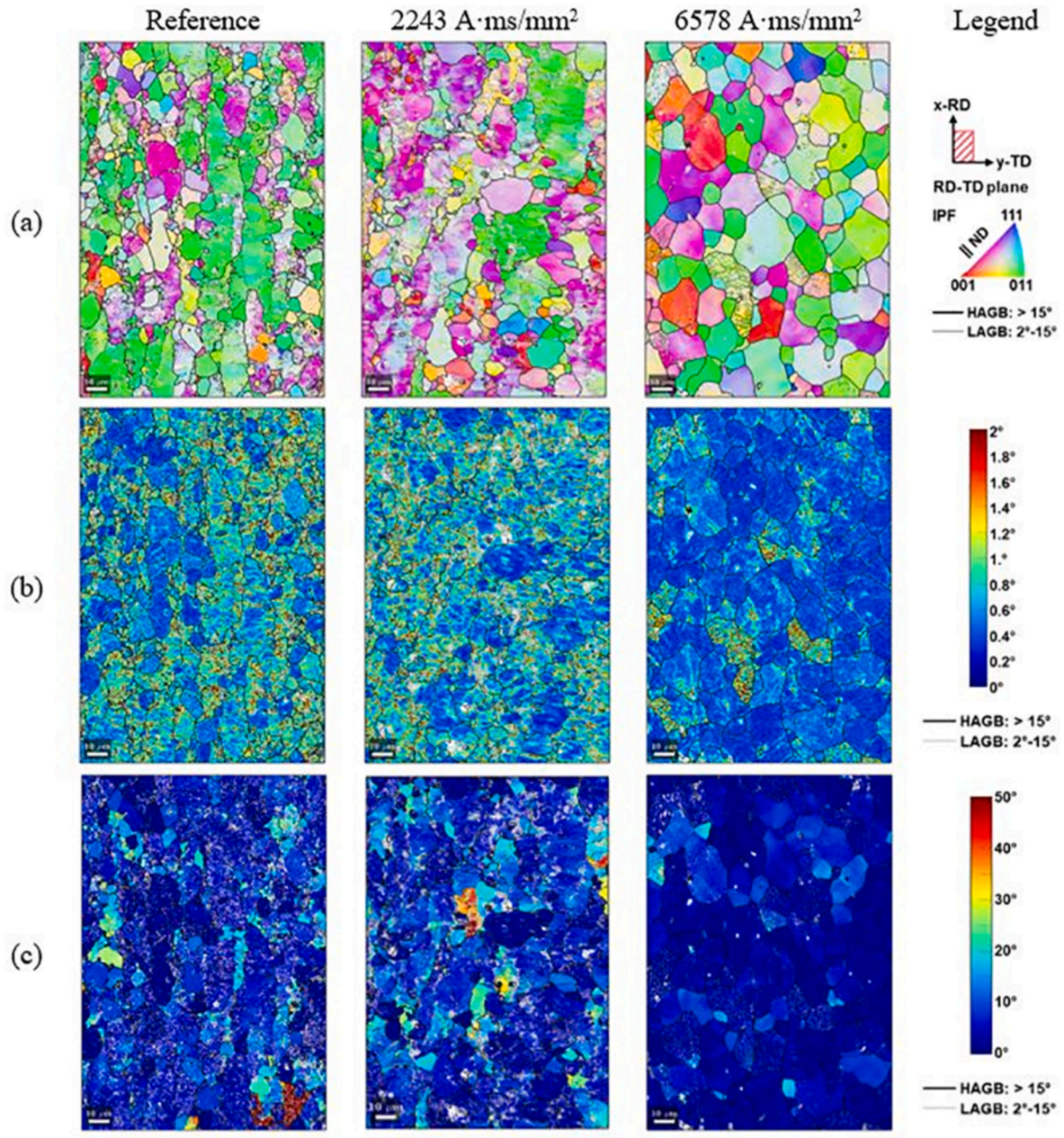

Fig. 7. Microstructure analyses of the reference (left), 2243 A ms/mm^2 (middle), and 6578 A ms/mm^2 (right) samples: a) crystal orientation maps; b) kernel average misorientation (KAM) maps and c) inner grain orientation spread (GOS) maps with high-angle grain boundaries (HAGBs) larger than 15° and low-angle grain boundaries (LAGBs) of 2–15°.

Table 2
Statistical microstructure parameters of the post-PFEPE samples.

	Reference	2243 A ms/mm^2	6578 A ms/mm^2
Grain number	4778	2323	2314
Grain size, mean value	19.43 μm	26.94 μm	23.59 μm
Grain size, standard deviation	15.44 μm	23.06 μm	12.50 μm
Grain shape factor, mean value	0.57	0.60	0.68
Grain shape factor, standard deviation	0.18	0.18	0.15
Grain shape tilt angle, mode value	0°/180°	0°/180°	0°/180°
Texture index	2.90	3.01	1.99

HAGBs (Fig. 8d). The average GOS value of each grain considered in the statistical analysis is typically smaller than 15° (Fig. 8e). The KAM value of each EBSD point, typically smaller than 2°, is also summarised for the statistical distribution (Fig. 8f). In addition, the grain size distribution can be fitted using the log-normal equation, while both grain shape parameters can be fitted using the beta distribution. The key fitting results are listed in Table 2.

The orientation distribution function (ODF) is calculated to compare the grain orientation distribution of the three samples. The ODF figures with φ_2 sections are given in Figs. 9–11, and the RD IPFs of all three samples are displayed in Fig. 12. The common fcc rolling texture can be seen in all specimens. The texture index [71] value used to characterise the ODF sharpness is defined using Equation (2):

$$t = -\oint f(g)^2 \mathrm{d}g. \tag{2}$$

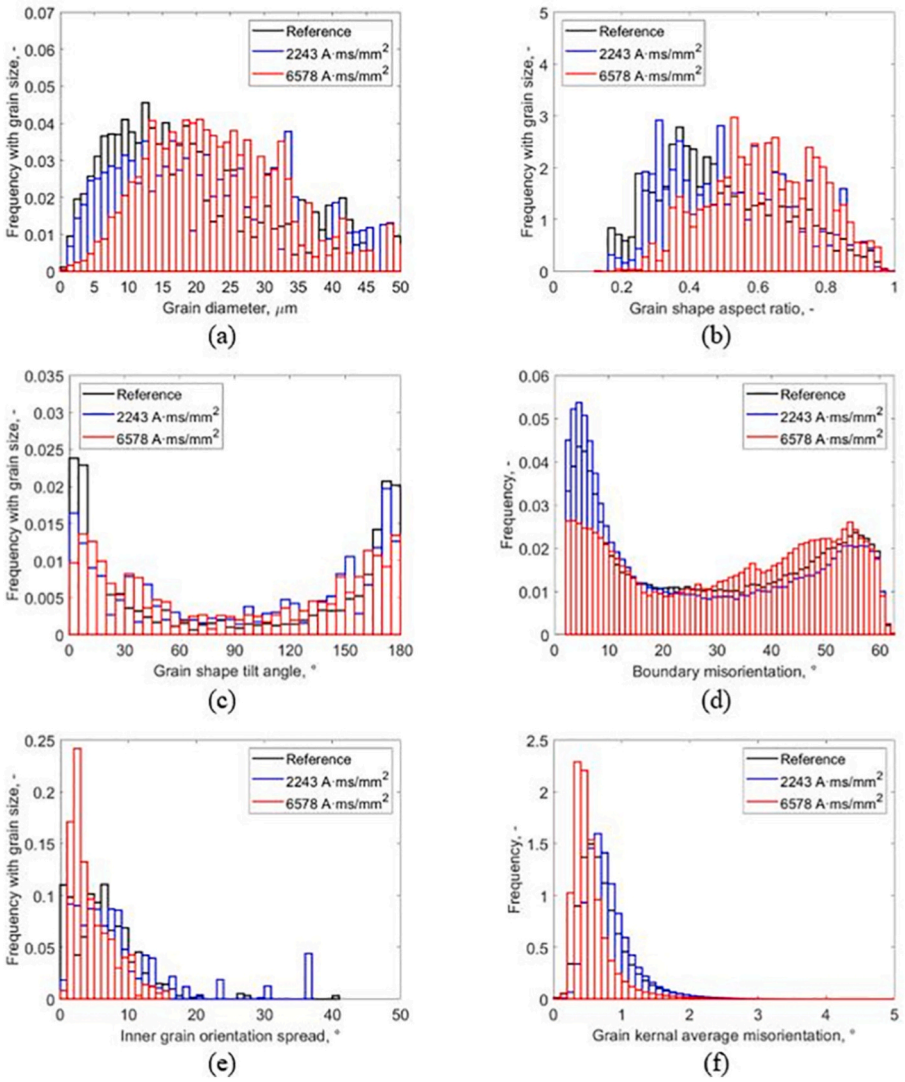

Fig. 8. Statistical microstructural features analyses of the post-PFEPE samples: a) grain size, b) grain shape factor, c) grain shape tilt angle, d) misorientation angle at the grain and sub-grain boundaries, e) mean grain orientation spread (GOS) angle and f) grain kernel average misorientation (KAM) angle.

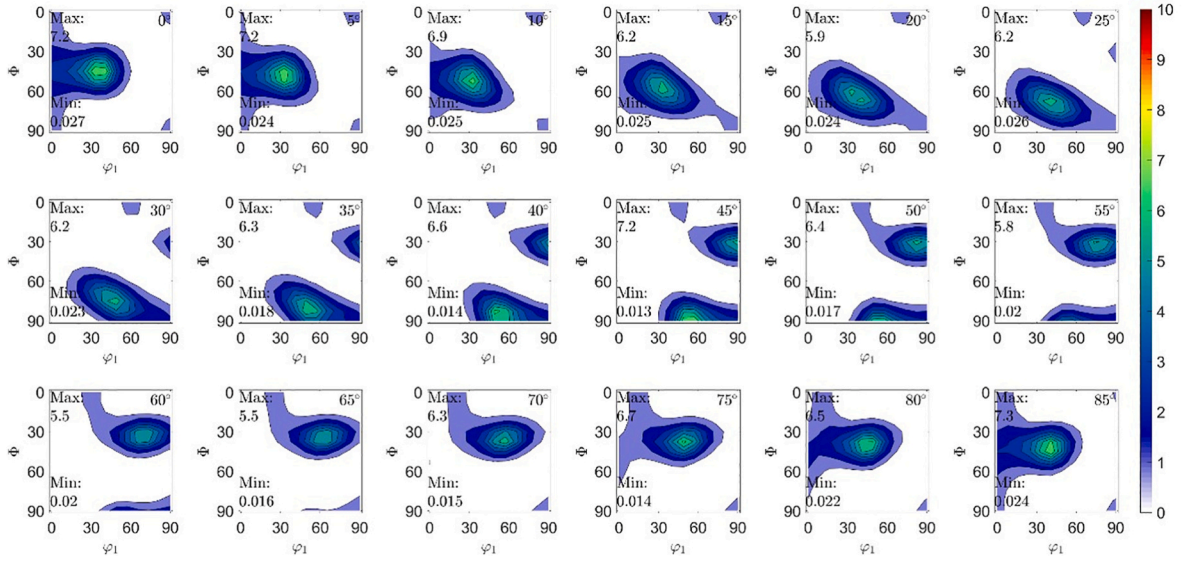

Fig. 9. Reference sample grain orientation distribution: orientation distribution function (ODF) figures with φ_2 sections.

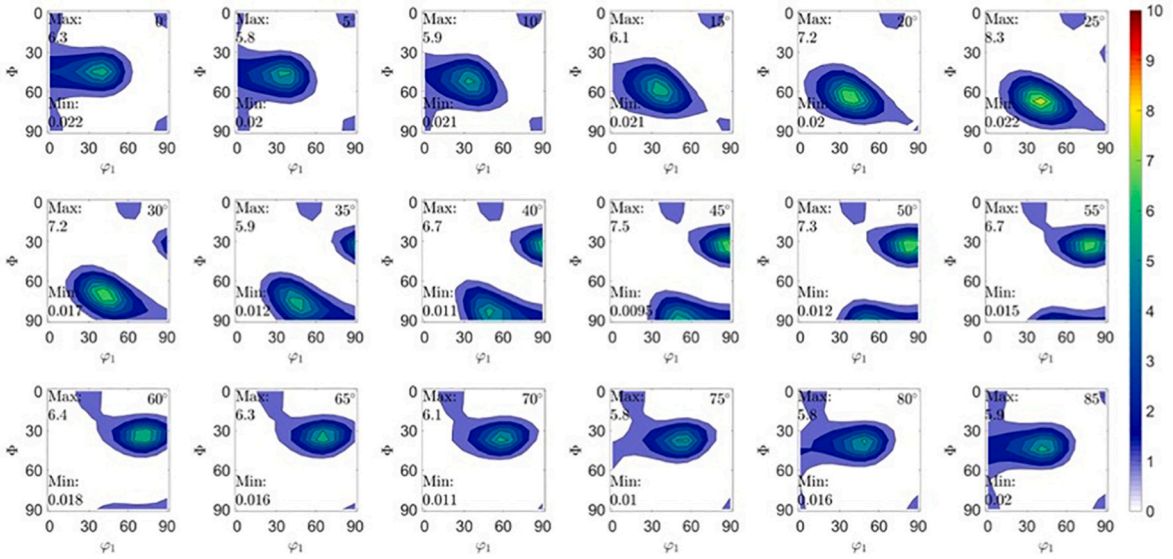

Fig. 10. Post-PFEPE 2243 A ms/mm^2 sample grain orientation distribution: orientation distribution function (ODF) figures with φ_2 sections.

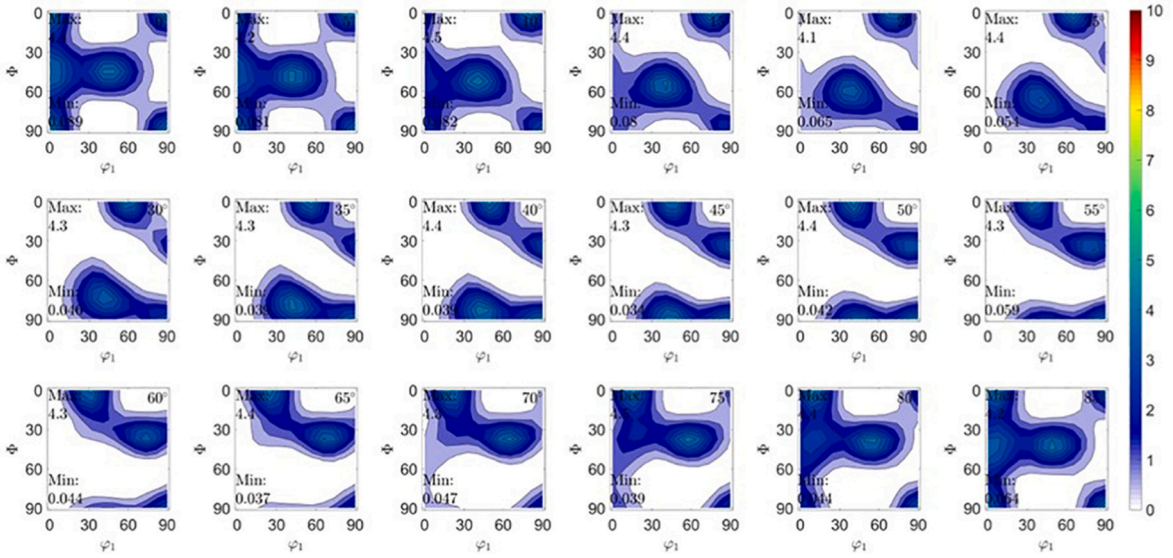

Fig. 11. Post-PFEPE 6578 A ms/mm^2 sample grain orientation distribution: orientation distribution function (ODF) figures with φ_2 sections.

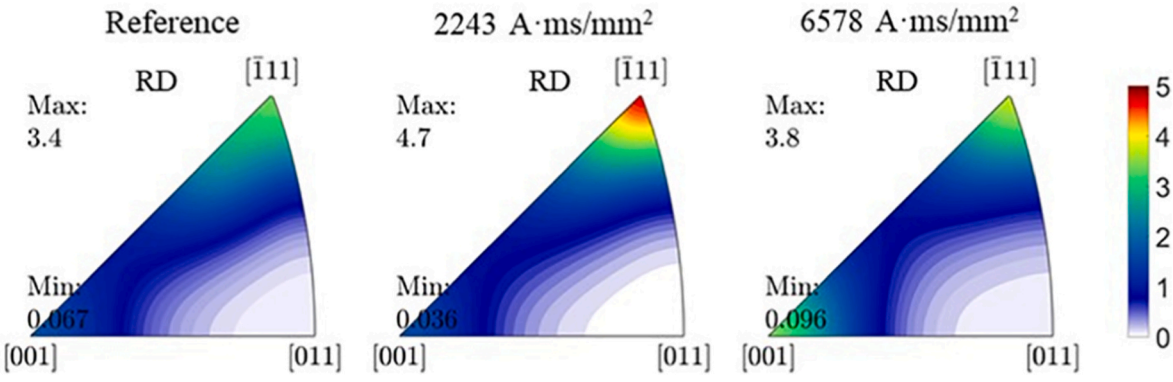

Fig. 12. Grain orientation distribution comparison: inverse pole figures (IPFs) for the reference, post-PFEPE 2243 A ms/mm^2 and 6578 A ms/mm^2 samples.

For orientation g, the density is $f(g)$ according to ODF. The random crystal orientation distribution is present with a texture index close to 1. The texture index value of each sample is listed in Table 2.

4. Discussion

Without discussing the phenomenon behind EPE's efficacy in modifying the dislocation distribution, Fig. 3 demonstrates that PFEPE is a valid technology for permanently reducing internal stresses in the material. Contrary to the expected outcome, an electrical pulse of 850 A ms/mm^2 was unable to rearrange the dislocation distribution to absorb the existing elastic strain. The first practical impact was measured following train pulses >2000 A ms/mm^2, achieving a ~10% stress decrease. At higher density pulse trains, energies around 4500 A ms/mm^2 led to decreases of around 30%, while decreases of about 65% were achieved with pulses of 5500 A ms/mm^2 density. An exponential trend can be observed between the pulse train's electric charge passing through the sample density and the resultant stress decrease. Working in these ranges using a single pulse means having to use pulse generators of ~10^4 A, depending on the area.

When analysing the peak temperatures achieved during the PFEPE process (see Fig. 4), it should be noted that the approximated solidus temperature of AA5754 is 876 K, and the liquidus is 915 K [73]. In the studied samples, the temperature reaches 300–350 K following low value pulses (<2000 A ms/mm^2) and increases linearly with the applied electrical charge passing through the sample to reach 750 K following pulses in the 6000 A ms/mm^2 range. Considering the typical recrystallisation temperature for aluminium alloys lies between 613 K and 673 K [74], pulse trains with energies >2000 A ms/mm^2 potentially lead to recrystallisation of the internal structure. However, the recrystallisation kinetics are driven not only by the peak temperature but also by the exposure time at these temperatures. Therefore, the sample's thermal temperature-time value (see Fig. 5) could be a more appropriate indicator. Contrary to the expected parabolic dependence of the Joule heating, an almost linear one has been measured. We don't have an explanation for this effect at the moment and further studied will be necessary on this matter.

As discussed in the introduction and methodology, recrystallisation could be an undesired side effect of PFEPE only if it substantially modifies the internal structure and, therefore, the material's performance at the mechanical level. Fig. 6 demonstrates the evolution of the material's strength (yield stress in this case) following PFEPE treatment. As expected, low value pulses <1000 A ms/mm^2 did not modify the material's strength (neither did they reveal any impact on stress reduction, Fig. 3). Therefore, the strength remains at ~184 MPa. A slight decrease (to ~175 MPa) is noted in the ~2200 A ms/mm^2 samples, and a slightly greater decrease (to 160 MPa) is observed in the ~4500 A ms/mm^2 samples. Nevertheless, in the <4800 A ms/mm^2 range, the material's strength is above the AA5754H22 virgin material's strength of 150 MPa (measured during the stress-relaxation test pre-strain), which is still valid from an industrial perspective. In contrast to these results, samples with an electrical charge passing through the sample density >4800 A ms/mm^2 exhibit a sudden critical decrease in mechanical performance as the strength decreases to 100 MPa.

In terms of microstructure, the elongated grain morphology with heterogeneous sub-grain structure can be observed in all three samples, although this is more obvious in the reference and 2243 A ms/mm^2 samples. This is because all the materials (including the reference sample) underwent the cold-rolling process and 2 mm uniaxial pre-strain (~6.25% of engineering strain). Grain-level analyses focused on the grain size, shape, orientation, and misorientation distribution, as illustrated in Fig. 8a–d and 9–12. In Fig. 8a and Table 2, it is evident from the smaller standard deviation that the 6578 A ms/mm^2 sample is most homogeneous. In addition, the post-PFEPE samples have a relatively larger mean grain size than the reference sample, and the 2243 A ms/mm^2 sample has the largest grain size. However, as the grain size measured by EBSD is a 2D representation on the RD-TD plane, and the grain length along ND is normally reduced due to rolling or tension along RD, the equivalent grain diameter on the RD-TD plane could not be determined to evaluate the actual grain size of the samples. Moreover, the relatively large standard deviations in the reference and 2243 A ms/mm^2 samples (i.e., close to their mean values) also indicate that the measured 2300 grains were insufficient to reveal the tendency of grain size change during the process.

Regarding the aspect ratio and the tilt angle, the grain shape distribution is almost the same in the reference and 2243 A ms/mm^2 samples (Fig. 8b and c and Table 2). The mean aspect ratio increases slightly as the pulse value increases, accompanied by a smaller standard deviation value. It is noted that extremely elongated grains with a small shape factor (aspect ratio $\leq$0.4) are much less frequent in the 6578 A ms/mm^2 sample, while the proportion of the semi-equiaxed grains (aspect ratio $\geq$0.9) gradually increases. Due to deformation, most grains are elongated along the rolling direction with a tilt angle of 0°/180°. The grain shape distribution indicates that grain morphology is more homogeneous in the sample with higher electrical pulse charge passing through the sample. In terms of the crystal orientation illustrated in Figs. 9–12, a typical fcc rolling texture (i.e., copper and sulfur components) is observed in all samples. The brass component is also observed in the reference and 2243 A ms/mm^2 samples. However, there is a slight deviation in the brass location in the 6578 A ms/mm^2 sample. In addition, the weak components close to Cube and Goss are also formed in the 6578 A ms/mm^2 sample, leading to a weak <100>//RD fibres (Fig. 12), which is the typical recrystallisation texture in fcc metals [75].

Moreover, the 2243 A ms/mm^2 sample reveals the strongest texture with the highest texture index and ODF current values, while the 6578 A ms/mm^2 sample has the weakest texture. It should be noted that the post-PFEPE samples are taken from the fcc material following tension. The formation of <111> and <100> fibres along the loading direction (i.e., RD) could also be caused by the deformation process. However, it is noted that the <111>//RD fibre is evident in all the samples, especially the 2243 A ms/mm^2 sample, while the <100>//RD fibre is more obvious in the 6578 A ms/mm^2 sample. Hence, the crystal orientation distribution findings could prove the occurrence of recrystallisation in the 6578 A ms/mm^2 sample. As demonstrated in Fig. 8d, the misorientation difference is primarily present in the LAGB section, indicating the highest LAGB fraction in the 2243 A ms/mm^2 sample and the lowest in the 6578 A ms/mm^2 sample. In contrast, the HAGB misorientation values of all three samples follow a similar distribution pattern, reaching a peak value around 55° and a cut-off at 62.8° due to their similar crystal orientation and the same cubic structure.

Sub-grain-level characterisation focused on various EBSD maps and statistical analyses of KAM, GOS, and LAGBs. In Fig. 7a, inner grain orientation heterogeneity is observed in most grains, regardless of the grain size, in the reference and 2243 A ms/mm^2 samples, while in the 6578 A ms/mm^2 sample, only a few large grains display heterogeneous inner grain crystal orientations with LAGBs. This finding is consistent with the KAM and local GOS maps in Fig. 7b and c. Most grains in the reference and 2243 A ms/mm^2 samples have higher local KAM and inner GOS values. The deviation between local crystal orientation and the mean grain orientation within a grain could reach 50° in these two samples. Severe lattice distortion and high dislocation densities are expected in these regions. While in the 6578 A ms/mm^2 sample, most grains have a homogeneous crystal orientation with local KAM values less than 0.8° and local GOS values lower than 15°. Only the grains with more LAGBs exhibit high KAM values. Furthermore, it is worth noting that the EBSD maps indicate clear LAGB networks in the post-PFEPE samples.

Conversely, in the reference sample, even with locally severe heterogeneous regions (high local KAM values), they generally do not form the sub-grain boundary network. This means the dislocations in the reference material generated by cold-forming and pre-straining processes could be more randomly distributed. With a possible recovery

process in the post-PFEPE samples, especially the sample with low electrical pulse charge passing through the sample, dislocation realignment occurred in the severely deformed grains to form density dislocation cell walls or sub-grain boundaries. The statistical analyses also support the findings of the local EBSD maps. As demonstrated in Fig. 8d–f, the 2243 A ms/mm^2 sample (blue bars) displays the highest proportion of LAGBs, as well as generally higher KAM and mean GOS values. The reference sample (black bars) shares a similar distribution with the 2243 A ms/mm^2 sample regarding values and corresponding frequency. However, a distinct difference in the fraction of LAGBs is also noted. The reference sample has fewer LAGBs than the 2243 A ms/mm^2 sample. In addition, a slightly lower frequency in the large GOS (10–50°) and KAM (0.8–2°) is also observed in the reference sample. The 6578 A ms/mm^2 sample (red bars) has a much less LAGB fraction and relatively lower KAM and mean GOS values. To further identify different grain behaviour, all grains can be divided into three groups with different mean GOS values, as indicated in Table 3. According to the literature, there are normally two methods of distinguishing between deformed and undeformed grains. Chen et al. [76] used a consistent misorientation angle combining a sub-grain structure investigation as the criteria for a CoCrFeMnNi high-entropy alloy. Grains with internal misorientation above 2° are deformed grains; otherwise, the grains are undeformed. In addition, sub-structured grains contain sub-cells with inner cell misorientation less than 2° but a cell boundary greater than 2°. Pan [81] employed multi-grades to classify grains in zirconium-containing aluminium alloys. Grains with mean GOS values lower than 1° were considered complete recrystallised grains, those with GOS ≥3°, deformed grains and those in between these values, partially recrystallised grains.

Considering the influence of initial cold-forming and pre-straining on the materials and the resulting complex sub-grain structures, 2° and 3° are chosen as the criteria to distinguish between undeformed and deformed grains in this study. Considering the possible phenomena (e.g., plastic deformation, recovery, and recrystallisation) caused by the cold-forming, tension-stress-relaxation, and post-forming electrical pulse processes, grains with a mean GOS smaller than 2° could be treated as initially undeformed grains or completely new-recrystallised grains. Grains with a mean GOS larger than 3° should be regarded as deformed grains without recrystallisation, while those in between 2° and 3° could be partly deformed or partially recrystallised grains. In addition, as the reference sample underwent the cold-forming and tension processes (the corresponding H22 + 2 mm pre-strain) without the electrical pulse train, there should be no recovery or recrystallisation. Table 3 demonstrates that the reference sample has the most undeformed grains. Following an electrical pulse train, the formation of density dislocation cells and LAGBs caused by a possible recovery in the 2243 A ms/mm^2 sample increased local inner grain heterogeneity and decreased the proportion of undeformed grains with GOS ≤2°. Furthermore, with increased electrical pulse charge passing through the sample, the 6578 A ms/mm^2 sample has more undeformed and partly deformed grains than the 2243 A ms/mm^2 sample. This finding suggests that recrystallisation could have occurred in the sample with high electrical pulse charge passing through the sample.

To sum up, a schematic summary of the microstructure evaluation is proposed (see Fig. 13). It is concluded that all the samples have experienced obvious plastic deformation, introducing an elongated grain shape, the typical rolling and uniaxial tension texture of fcc metals and higher dislocation density, which is especially evident in the reference and 2243 A ms/mm^2 samples. Possible recovery or recrystallisation caused by the electrical pulse train had substantial effects on the dislocation density (i.e., KAM values) in the post-PFEPE samples. Following relatively low pulse value, dislocation realignment formed strong, dense dislocation walls and low-angle sub-grain boundaries in the 2243 A ms/mm^2 sample, resulting in more deformed or partly deformed grains with a mean GOS angle above 2°. Following high pulse value, the 6578 A ms/mm^2 sample could have also undergone recrystallisation to present unexpected microstructure changes at both the grain and sub-grain levels, including reduced dislocation density, dissipated LAGBs, more completely or partly recrystallised grains, and relatively weak texture but obvious fcc recrystallisation texture components. To prove that the inner grain behaviour is caused by the stress-relaxation plus PFEPE, more advanced material techniques should be considered in future studies, for example, using transmission electron microscopy to characterise the dislocation density and morphology.

Table 3
Fraction of grains with different mean grain orientation spread (GOS) values.

Mean GOS range	Reference	2243 A ms/mm^2	6578 A ms/mm^2
GOS ≤2°	20.86%	11.03%	17.92%
2 < GOS <3°	4.27%	9.03%	24.18%
GOS ≥3°	74.87%	79.94%	57.90%

According to current microstructure analyses, the distinct lower yield strength and the reduction in internal stresses in the 6578 A ms/mm^2 sample should be attributed to its homogeneous grain and sub-grain structure, including the lower dislocation density, inner grain orientation heterogeneity, and low-angle grain boundary fraction. Fig. 6 demonstrates that recrystallisation could be expected following pulses with electric charge passing through the sample densities of >4800 A ms/mm^2, which has previously introduced a different microstructure to the initial material. For samples with low value pulses, mechanical properties such as yield strength and grain-level microstructure are not distinctly affected. In light of these results, a 30% reduction in internal stresses could be achieved without critically modifying the material's microstructure and, therefore, its mechanical performance.

5. Conclusions

This study has investigated PFEPE's capacity to reduce internal stresses in pre-deformed AA5754H22 material. Based on the above results, the following conclusions are presented:

- PFEPE is a valid technique for reducing internal stresses in AA5754H22 material.
- An exponential relationship between decreased stress and electrical charge passing through the sample density can be observed; pulses ~2200 A ms/mm^2 led to a 10% reduction, pulses ~4500 A ms/mm^2 produced a 30% reduction, and pulses ~6500 A ms/mm^2 resulted in a 60% reduction.
- The constructed pulse generator (HCDH) was unable to supply the necessary electric charge passing through the sample (>2200 A ms/mm^2) in a single pulse (<1 ms). Therefore multiple pulses (pulse trains) were required for the study. However, we believe that a single pulse of this magnitude should lead to similar reduction rates.
- Most of the effective pulses (>2200 A ms/mm^2) generate temperatures above the recrystallisation temperature range. However, due to the speed of the thermal effect, it appears that only pulses above 4500 A ms/mm^2 lead to major microstructural changes affecting the mechanical performance of the material.
- The sample with low electrical pulse charge passing through the sample (2243 A ms/mm^2) retains a similar grain-level microstructure, inner grain morphology and resulting mechanical properties compared to the initial material, yet with a 10% stress reduction.
- Recovery and recrystallisation could have occurred in the sample with high electrical pulse charge passing through the sample (6578 A ms/mm^2). The homogenous grain structure with reduced dislocation density, fewer LAGBs, and weak texture indicates a different microstructure than the reference and 2243 A ms/mm^2 samples, explaining its distinctly lower yield strength and internal stress.

This study also acknowledges the following limitations and open questions:

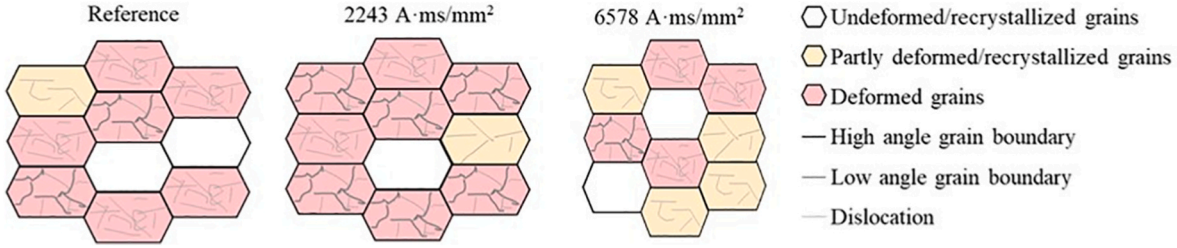

Fig. 13. Schematic representation of grain morphology and dislocation dynamics during the PFEPE process (RX grains: recrystallised grains).

- The study has demonstrated PFEPE's capacity to reduce internal stresses in AA5754H22. However, it has not been validated that this reduction could effectively reduce springback in the material. Therefore, further investigation is required.
- Previous authors have disagreed regarding the micro-phenomena responsible for EPE, such as electron wind [77,78], magneto-plasticity [79], the Joule effect [69] and atomic bond dissolution [80]. Since this work does not clarify the micro-phenomenon responsible for the PFEPE, further analysis is necessary.
- It has to be taken into account that following previous authors terminology/methodology the density has been calculated considering the whole sample section without taken into account the skin-effect. To consider the skin-effect further studies will have to be conducted.
- In order to work towards the up-scaling of the technology still the question of how to apply the pulses through thickness and if the measured stress-relaxations have an impact on the global springback are still up to answer and further studies will be necessary on these topics.

CRediT authorship contribution statement

Wenqi Liu: Methodology, Software, Formal analysis, Investigation, Writing – original draft, Writing – review & editing, Visualization. **Nagore Otegi:** Validation, Investigation. **Ana Orallo:** Investigation. **Manex Barrenetxea:** Investigation. **Iosu Aizpuru:** Software. **Junhe Lian:** Validation, Resources, Writing – review & editing, Supervision. **Joseba Mendiguren:** Conceptualization, Methodology, Formal analysis, Resources, Writing – original draft, Writing – review & editing, Supervision, Project administration, Funding acquisition.

Declaration of competing interest

The authors declare that they have no known competing financial interests or personal relationships that could have appeared to influence the work reported in this paper.

Data availability

Data will be made available on request.

Acknowledgements

We wish to acknowledge the POSTELEC, *Reducción de springback mediante Post-forming Electro-plastic Effect* project funded by the Education Department of the Basque Government (Spain), within the financial aid Basic and Applied Research, reference number PI2017-47. We also wish to acknowledge Xabier Lopez de Murillas for his experimental skills.

References

[1] N. Jackson, Lightweight Vehicle and Powertrain Structures Roadmap 2020, 2021. London.
[2] J. Hirschi, Recent development in aluminium for automotive applications, Trans. Nonferrous Metals Soc. China 24 (2014), https://doi.org/10.1016/S1003-6326(14)63305-7, 1995–2002.
[3] J. Cao, M. Banu, Opportunities and challenges in metal forming for lightweighting: review and future work, J. Manuf. Sci. Eng. 142 (2020), https://doi.org/10.1115/1.4047732.
[4] A. Lakshmi, T. Buddi, R. Subbiah, C. Bandhavi, Formability studies of automotive aluminium alloy sheet series: a review, E3S Web Confe. 184 (2020), 01036, https://doi.org/10.1051/e3sconf/202018401036.
[5] R.H. Wagoner, J.F. Wang, M. Li, Springback, Metalworking: Sheet Forming, 2018, pp. 733–755, https://doi.org/10.31399/asm.hb.v14b.a0005131.
[6] J. Mendiguren, J.J. Trujillo, F. Cortés, L. Galdos, An extended elastic law to represent non-linear elastic behaviour: application in computational metal forming, Int. J. Mech. Sci. 77 (2013) 57–64.
[7] A. Maia, E. Ferreira, M.C. Oliveira, L.F. Menezes, A. Andrade-Campos, Numerical optimization strategies for springback compensation in sheet metal forming, in: Computational Methods and Production Engineering, Elsevier, 2017, pp. 51–82, https://doi.org/10.1016/B978-0-85709-481-0.00003-3.
[8] Z. Bing, C. Guo, Z. Chun, N.I. Jia, A. Welding, A. Shenyang, A. Corporation, Warm forming behaviour of high strength aluminum alloys AA7075. https://doi.org/10.1016/S1003, 2011, 6326, 1-5.
[9] M. Merklein, M. Wieland, M. Lechner, S. Bruschi, A. Ghiotti, Hot stamping of boron steel sheets with tailored properties: a review, Hot Stamping 228 (2016) 11–24, https://doi.org/10.1016/j.jmatprotec.2015.09.023.
[10] O.A. Troitskii, Effect of the electron state of a metal on its mechanical properties and the phenomenon of electroplasticity, Strength Mater. 9 (1977) 35–45.
[11] Z. Cai, X. Huang, Residual stress reduction by combined treatment of pulsed magnetic field and pulsed current, Mater. Sci. Eng. A 528 (2011) 6287–6292.
[12] H. Conrad, Electroplasticity in metals and ceramics, Mater. Sci. Eng. A 287 (2000) 276–287, https://doi.org/10.1016/S0921-5093(00)00786-3.
[13] H. Conrad, Thermally activated plastic flow of metals and ceramics with an electric field or current, Mater. Sci. Eng., A 322 (2002) 100–107, https://doi.org/10.1016/S0921-5093(01)01122-4.
[14] Y. Jiang, L. Guan, G. Tang, C. Shek, Z. Zhang, Influence of electropulsing treatment on microstructure and mechanical properties of cold-rolled Mg-9Al-1Zn alloy strip, Mater. Sci. Eng. A 528 (2011) 5627–5635. http://www.sciencedirect.com/science/article/pii/S0921509311003959.
[15] K. Liu, X. Dong, H. Xie, F. Peng, Effect of pulsed current on the deformation behavior of AZ31B magnesium alloy, Mater. Sci. Eng. A 623 (2015) 97–103, https://doi.org/10.1016/j.msea.2014.11.039.
[16] K. Liu, X. Dong, H. Xie, Y. Wu, F. Peng, Influence of pulsed current on deformation mechanism of AZ31B sheets during tension, J. Alloys Compd. 676 (2016) 106–112, https://doi.org/10.1016/j.jallcom.2016.03.149.
[17] S.J. Kim, S.D. Kim, D. Yoo, J. Lee, Y. Rhyim, D. Kim, Evaluation of the athermal effect of electric pulsing on the recovery behavior of magnesium alloy, Metall. Mater. Trans. A., Phys. Metall. Mater. Sci. 47 (2016) 6368–6373, https://doi.org/10.1007/s11661-016-3804-0.
[18] J. Lee, S.J. Kim, M.G. Lee, J.H. Song, S. Choi, H.N. Han, D. Kim, Experimental and numerical study on the deformation mechanism in AZ31B Mg alloy sheets under pulsed electric-assisted tensile and compressive tests, Metall. Mater. Trans. A., Phys. Metall. Mater. Sci. 47 (2016) 2783–2794, https://doi.org/10.1007/s11661-016-3492-9.
[19] T.T. Nguyen, T.V. Nguyen, S.-T. Hong, M.-J. Kim, H.N. Han, F. Morestin, The effect of short duration electric current on the quasi-static tensile behavior of magnesium AZ31 alloy, Adv. Mater. Sci. Eng. (2016), 9560413, https://doi.org/10.1155/2016/9560413.
[20] X. Wang, J. Xu, D. Shan, B. Guo, J. Cao, Modeling of thermal and mechanical behavior of a magnesium alloy AZ31 during electrically-assisted micro-tension, Int. J. Plast. 85 (2016) 230–257, https://doi.org/10.1016/j.ijplas.2016.07.008.
[21] X. Wang, J. Xu, Z. Jiang, W. Le Zhu, D. Shan, B. Guo, J. Cao, Size effects on flow stress behavior during electrically-assisted micro-tension in a magnesium alloy AZ31, Mater. Sci. Eng. A (2016), https://doi.org/10.1016/j.msea.2016.02.064.
[22] H. Xie, X. Dong, Z. Ai, Q. Wang, F. Peng, K. Liu, F. Chen, J. Wang, Experimental investigation on electrically assisted cylindrical deep drawing of AZ31B magnesium alloy sheet, Int. J. Adv. Manuf. Technol. (2016), https://doi.org/10.1007/s00170-015-8246-0.
[23] H.J. Jeong, M.J. Kim, J.W. Park, C.D. Yim, J.J. Kim, O.D. Kwon, P.P. Madakashira, H.N. Han, Effect of pulsed electric current on dissolution of Mg17Al12phases in as-extruded AZ91 magnesium alloy, Mater. Sci. Eng. A (2017), https://doi.org/10.1016/j.msea.2016.12.103.

[24] K. Liu, X. Dong, W. Shi, Effect of pulsed current on AZ31B magnesium sheets during annealing, Trans. Nonferrous Metals Soc. China 29 (2019) 735–740, https://doi.org/10.1016/S1003-6326(19)64983-6.
[25] X. Wang, C. Xu, Y. Li, B. Wang, Respective roles of the thermal and electromigration effect in AZ31 Mg alloy during low-frequency electropulsing tension, J. Alloys Compd. (2020) 846, https://doi.org/10.1016/j.jallcom.2020.156074.
[26] X. Liu, S. Lan, J. Ni, Experimental study of electro-plastic effect on advanced high strength steels, Mater. Sci. Eng. A 582 (2013) 211–218, https://doi.org/10.1016/j.msea.2013.03.092.
[27] W. Kim, K.H. Yeom, N.T. Thien, S.T. Hong, B.K. Min, S. Ik Oh, M.J. Kim, H.N. Han, H.W. Lee, Electrically assisted blanking using the electroplasticity of ultra-high strength metal alloys, CIRP Ann. - Manuf. Technol. 63 (2014) 273–276, https://doi.org/10.1016/j.cirp.2014.03.064.
[28] N.T. Thien, Y.H. Jeong, S.T. Hong, M.J. Kim, H.N. Han, M.G. Lee, Electrically assisted tensile behavior of complex phase ultra-high strength steel, Int. J. Precis. Eng. Manufact. Green Technol. (2016), https://doi.org/10.1007/s40684-016-0041-3.
[29] H. Xie, X. Dong, K. Liu, Z. Ai, F. Peng, Q. Wang, F. Chen, J. Wang, Experimental investigation on electroplastic effect of DP980 advanced high strength steel, Mater. Sci. Eng., A 637 (2015) 23–28, https://doi.org/10.1016/j.msea.2015.04.016.
[30] M.-S. Kim, N.T. Vinh, H.-H. Yu, S.-T. Hong, H.-W. Lee, M.-J. Kim, H.N. Han, J. T. Roth, Effect of electric current density on the mechanical property of advanced high strength steels under quasi-static tensile loads, Int. J. Precis. Eng. Manuf. (2014), https://doi.org/10.1007/s12541-014-0458-y.
[31] T. Jiang, L. Peng, P. Yi, X. Lai, Investigation of deformation behavior of ss304 and pure copper subjected to electrically assisted forming process, J. Manufact. Sci. Eng. Trans. ASME 139 (2017), https://doi.org/10.1115/1.4033904.
[32] A. Khal, B.J. Ruszkiewicz, L. Mears, Springback evaluation of 304 stainless steel in an electrically assisted air bending operation. https://doi.org/10.1115/msec2016-8736, 2016.
[33] A.J. Sánchez Egea, H.A. González Rojas, D.J. Celentano, J. Jorba Peiró, Mechanical and metallurgical changes on 308L wires drawn by electropulses, Materials and Design. https://doi.org/10.1016/j.matdes.2015.11.067, 2016.
[34] A.J. Sánchez Egea, J.J. Peiró, J.W. Signorelli, H.A. González Rojas, D.J. Celentano, On the microstructure effects when using electropulsing versus furnace treatments while drawing inox 308L, J. Mater. Res. Technol. 8 (2019) 2269–2279, https://doi.org/10.1016/j.jmrt.2019.03.007.
[35] H.J. Jeong, M.J. Kim, S.J. Choi, J.W. Park, H. Choi, V.T. Luu, S.T. Hong, H.N. Han, Microstructure reset-based self-healing method using sub-second electric pulsing for metallic materials, Appl. Mater. Today 20 (2020), 100755, https://doi.org/10.1016/j.apmt.2020.100755.
[36] A.J. Sánchez Egea, H.A. González Rojas, D.J. Celentano, J.A. Travieso-Rodríguez, J. Llumà I Fuentes, Electroplasticity-assisted bottom bending process, J. Mater. Process. Technol. 214 (2014) 2261–2267. http://www.sciencedirect.com/science/article/pii/S0924013614001630.
[37] Z. Tang, H. Du, L. Lang, S. Jiang, J. Chen, J. Zhang, Experimental investigation into the electropulsing assisted punching process of 2024T4 aluminum alloy sheet, J. Mater. Process. Technol. 132 (2018), 21004.
[38] Z. Tang, H. Du, K. Tao, J. Chen, J. Zhang, Effect of electropulsing on edge stretchability and corrosion resistance near the punched edge of a 2024T4 aluminum alloy sheet, J. Mater. Process. Technol. (2019), https://doi.org/10.1016/j.jmatprotec.2018.08.035.
[39] S.T. Hong, Y.H. Jeong, M.N. Chowdhury, D.M. Chun, M.J. Kim, H.N. Han, Feasibility of Electrically Assisted Progressive Forging of Aluminum 6061-T6 Alloy, CIRP Annals - Manufacturing Technology, 2015, https://doi.org/10.1016/j.cirp.2015.04.084.
[40] J. Jung, Y. Ju, Y. Morita, Y. Toku, Y. Uematsu, Delaying effect of high-density electric current on fatigue crack growth in A6061-T6 aluminum alloy, Mater. Trans. 57 (2016) 2104–2109, https://doi.org/10.2320/matertrans.M2016240.
[41] D. Pan, Y. Wang, Q. Guo, D. Zhang, X. Xu, Y. Zhao, Grain refinement of Al–Mg–Si alloy without any mechanical deformation and matrix phase transformation via cyclic electro-pulsing treatment, Mater. Sci. Eng. A 807 (2021), 140916, https://doi.org/10.1016/j.msea.2021.140916.
[42] S. Hameed, H. González Rojas, J. Perat Benavides, A. Nápoles Alberro, A. Sánchez Egea, Influence of the regime of electropulsing-assisted machining on the plastic deformation of the layer being cut, Materials 11 (2018) 886, https://doi.org/10.3390/ma11060886.
[43] J. Tiwari, P. Pratheesh, O.B. Bembalge, H. Krishnaswamy, M. Amirthalingam, S. K. Panigrahi, Microstructure dependent electroplastic effect in AA 6063 alloy and its nanocomposites, J. Mater. Res. Technol. 12 (2021) 2185–2204, https://doi.org/10.1016/j.jmrt.2021.03.112.
[44] K. Chen, L. Zhan, W. Yu, Rapidly modifying microstructure and mechanical properties of AA7150 Al alloy processed with electropulsing treatment, J. Mater. Sci. Technol. 95 (2021) 172–179, https://doi.org/10.1016/j.jmst.2021.03.060.
[45] H. Zhang, X. Zhang, Suppressing or promoting: the effect of coupled electron-heat field on serration behavior, J. Alloys Compd. 818 (2020), 152920, https://doi.org/10.1016/j.jallcom.2019.152920.
[46] X. Zhang, S. Zhou, H. Zhang, X. Liu, H. Yang, Lüders strain of the fine-grained material under the electric current, Mater. Sci. Eng. A 825 (2021), 141924, https://doi.org/10.1016/j.msea.2021.141924.
[47] M.J. Kim, K. Lee, K.H. Oh, I.S. Choi, H.H. Yu, S.T. Hong, H.N. Han, Electric current-induced annealing during uniaxial tension of aluminum alloy, Scripta Mater. 75 (2014) 58–61.
[48] J.-H. Roh, J.-J. Seo, S.-T. Hong, M.-J. Kim, H.N. Han, J.T. Roth, The mechanical behavior of 5052-H32 aluminum alloys under a pulsed electric current, Honor of Kwansoo Chung 58 (2014) 84–99. http://www.sciencedirect.com/science/article/pii/S0749641914000345.
[49] M. Kim, J. Song, H. Huh, Effect of pre-strain on tensile properties of Al5052-H32 under an electropulsing condition, in: Procedia Engineering, 2017, https://doi.org/10.1016/j.proeng.2017.10.790.
[50] M.J. Kim, S. Yoon, S. Park, H.J. Jeong, J.W. Park, K. Kim, J. Jo, T. Heo, S.T. Hong, S.H. Cho, Y.K. Kwon, I.S. Choi, M. Kim, H.N. Han, Elucidating the origin of electroplasticity in metallic materials, Appl. Mater. Today 21 (2020), 100874, https://doi.org/10.1016/j.apmt.2020.100874.
[51] A.A. Shibkov, A.A. Denisov, M.A. Zheltov, A.E. Zolotov, M.F. Gasanov, The electric current-induced suppression of the Portevin - Le Chatelier effect in Al-Mg alloys, Mater. Sci. Eng., A 610 (2014) 338–343. http://www.sciencedirect.com/science/article/pii/S0921509314006510.
[52] C.L. Liang, K.L. Lin, The microstructure and property variations of metals induced by electric current treatment: a review, Mater. Char. 145 (2018) 545–555, https://doi.org/10.1016/j.matchar.2018.08.058.
[53] T.J. Grimm, L. Mears, Effect of power supply type on the electroplastic effect, J. Manuf. Process. 56 (2020) 1263–1269, https://doi.org/10.1016/j.jmapro.2020.04.020.
[54] B. Ruszkiewicz, T. Grimm, I. Ragai, L. Mears, J.T. Roth, A review of electrically-assisted manufacturing with emphasis on modeling and understanding of the electroplastic effect, J. Manuf. Sci. Eng. (2017), https://doi.org/10.1115/1.4036716.
[55] K. Mori, S. Saito, S. Maki, Warm and hot punching of ultra high strength steel sheet, CIRP Annals 57 (2008) 321–324, https://doi.org/10.1016/j.cirp.2008.03.125.
[56] B.A. Behrens, S. Hübner, S. Schrödter, J. Uhe, Conductive heating opens up various new opportunities in hot stamping, in: Proceedings of 5th International Conference on Accuracy in Forming Technology, ICAFT 2015), 2015, pp. 157–174.
[57] K. Mori, T. Maeno, K. Mongkolkaji, Tailored die quenching of steel parts having strength distribution using bypass resistance heating in hot stamping, J. Mater. Process. Technol. 213 (2013) 508–514. http://www.sciencedirect.com/science/article/pii/S0924013612003019.
[58] J. Song, I. Jang, S. Gwak, W. Noh, J. Lee, G. Bae, D. Kim, Effect of pulsed currents on the springback reduction of ultra-high strength steels, in: Procedia Engineering, 2017, https://doi.org/10.1016/j.proeng.2017.10.788.
[59] W. Li, Y. Shen, H. Liu, Y. Wang, W. Zhu, C. Xie, Non-octahedral-like dislocation glides in aluminum induced by athermal effect of electric pulse, J. Mater. Res. 31 (2016) 1193–1200.
[60] G. Gerstein, F. Körkemeyer, A. Dalinger, S. Zaefferer, H.J. Maier, Anomalous twinning in AZ 31 magnesium alloy during electrically assisted forming, Mater. Lett. 255 (2019), 126516, https://doi.org/10.1016/j.matlet.2019.126516.
[61] Y. Zhao, L. Peng, X. Lai, Influence of the electric pulse on springback during stretch U-bending of Ti6Al4V titanium alloy sheets, J. Mater. Process. Technol. 261 (2018) 12–23, https://doi.org/10.1016/j.jmatprotec.2018.05.030.
[62] J. Olaizola, E. Esteban, J. Trinidad, A. Iturrospe, L. Galdos, J.M. Abete, E.S. de Argandona, Integral design and manufacturing methodology of a reduced-scale servo press, IEEE ASME Trans. Mechatron. 26 (2021) 2418–2428, https://doi.org/10.1109/TMECH.2020.3039678.
[63] J. Olaizola, C.-S. Bouganis, E.S. de Argandona, A. Iturrospe, J.M. Abete, Real-time servo press force estimation based on dual particle filter, IEEE Trans. Ind. Electron. 67 (2020) 4088–4097, https://doi.org/10.1109/TIE.2019.2921292.
[64] C. Bolay, P. Essig, C. Kaminsky, J. Hol, P. Naegele, R. Schmidt, Friction modelling in sheet metal forming simulations for aluminium body parts at Daimler AG, IOP Conf. Ser. Mater. Sci. Eng. 651 (2019), 012104, https://doi.org/10.1088/1757-899X/651/1/012104.
[65] P. Essig, M. Liewald, C. Bolay, T. Schubert, Digital process support in toolmaking by using optical metrology, IOP Conf. Ser. Mater. Sci. Eng. (2019) 651, https://doi.org/10.1088/1757-899X/651/1/012026.
[66] P. Essig, M. Liewald, M. Burkart, M. Beck, Modelling real contact areas caused by material straining effects in sheet metal forming simulation, ESAFORM 2021 (2021), https://doi.org/10.25518/esaform21.1954.
[67] A. Zabala, I. Llavori, E. Sáenz de Argandoña, J. Mendiguren, Towards the automation of the die spotting process: contact blue pattern decryption, J. Manuf. Process. 58 (2020) 1285–1296, https://doi.org/10.1016/j.jmapro.2020.09.022.
[68] P. Leo, S. D'Ostuni, G. Casalino, Hybrid welding of AA5754 annealed alloy: role of post weld heat treatment on microstructure and mechanical properties, Mater. Des. 90 (2016) 777–786, https://doi.org/10.1016/j.matdes.2015.10.150.
[69] W.A. Salandro, J.J. Jones, C. Bunget, L. Mears, J.T. Roth, in: Electrically Assisted Forming, Springer International Publishing, Cham, 2015, https://doi.org/10.1007/978-3-319-08879-2.
[70] F. Bachmann, R. Hielscher, H. Schaeben, Texture analysis with MTEX – free and open source software toolbox, Solid State Phenom. 160 (2010) 63–68. https://doi.org/10.4028/www.scientific.net/SSP.160.63.
[71] W. Liu, J. Lian, N. Aravas, S. Münstermann, A strategy for synthetic microstructure generation and crystal plasticity parameter calibration of fine-grain-structured dual-phase steel, Int. J. Plast. 126 (2020), 102614, https://doi.org/10.1016/j.ijplas.2019.10.002.
[72] J. Lian, W. Liu, X. Gastañares, R. Juan, J. Mendiguren, Plasticity evolution of an aluminum-magnesium alloy under abrupt strain path changes, Int. J. Material Form. 15 (2022) 40, https://doi.org/10.1007/s12289-022-01692-6.
[73] H. Zhang, J. Senkara, X. Wu, Suppressing cracking in resistance welding AA5754 by mechanical means, J. Manuf. Sci. Eng. 124 (2002) 79–85, https://doi.org/10.1115/1.1418693.
[74] R. Singh, Heat treatment of steels, in: Applied Welding Engineering, Elsevier, 2016, pp. 111–124, https://doi.org/10.1016/B978-0-12-804176-5.00012-8.

[75] O. Engler, V. Randle, Introduction to Texture Analysis, CRC Press, 2009, https://doi.org/10.1201/9781420063660.
[76] B.R. Chen, A.C. Yeh, J.W. Yeh, Effect of one-step recrystallization on the grain boundary evolution of CoCrFeMnNi high entropy alloy and its subsystems, Sci. Rep. 6 (2016), 22306, https://doi.org/10.1038/srep22306.
[77] M. Molotskii, V. Fleurov, Magnetic effects in electroplasticity of metals, Phys. Rev. B 52 (1995) 15829–15834, https://doi.org/10.1103/PhysRevB.52.15829.
[78] A.F. Sprecher, S.L. Mannan, H. Conrad, Overview no. 49, Acta Metall. 34 (1986) 1145–1162, https://doi.org/10.1016/0001-6160(86)90001-5.
[79] F.R.N. Nabarro, Theory of Crystal Dislocations, At the Clarendon Press, 1967.
[80] B.J. Ruszkiewicz, L. Mears, Temperature-controlled forming of 7075-T6 aluminum using linearly decaying direct electric current, J. Manuf. Sci. Eng. 138 (2016), https://doi.org/10.1115/1.4033902.
[81] S. Pan, Precipitation Behavior and Dispersion-Strengthening Mechanism of Nano-Sized Dispersoids in Zirconium-Containing Aluminium Alloys, Doctoral thesis, at University of Science and Technology Beijing, 2022, https://doi.org/10.26945/d.cnki.gbjku.2022.000028.